Materials & Design 186 (2020) 108288

Contents lists available at ScienceDirect

Materials & Design

journal homepage: www.elsevier.com/locate/matdes

Micropore evolution in additively manufactured aluminum alloys under heat treatment and inter-layer rolling

Jianglong Gu [a, b], Shouliang Yang [a], Minjie Gao [a], Jing Bai [c, *], Yuchun Zhai [c], Jialuo Ding [d]

[a] State Key Laboratory of Metastable Materials Science and Technology, Yanshan University, Qinhuangdao, 066004, PR China
[b] Hebei Key Laboratory for Optimizing Metal Product Technology and Performance, Yanshan University, Qinhuangdao, 066004, PR China
[c] School of Materials Science and Engineering, Northeastern University, Shenyang, 110819, PR China
[d] Welding Engineering and Laser Processing Centre, Cranfield University, Bedfordshire, MK430AL, UK

HIGHLIGHTS

- Rolling was introduced to additive manufacture to eliminate micropores.
- Micropores number, volume, size, and roundness decreased with increasing loads.
- Fine and spherical micropores homogeneously distributed by hybrid technique.
- Evolution mechanisms include H precipitation, microvoid formation, pore reopening.

GRAPHICAL ABSTRACT

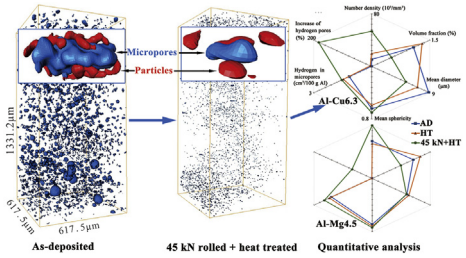

ARTICLE INFO

Article history:
Received 28 August 2019
Received in revised form
30 September 2019
Accepted 17 October 2019
Available online 28 October 2019

Keywords:
Directed energy deposition
Wire + arc additive manufacture
Micropores
Aluminum alloy
X-ray computed tomography

ABSTRACT

The application of wire + arc additively manufactured (WAAM) aluminum alloys has been restricted by the porosity defect, which is generally detrimental to the mechanical properties. Suppressing of micropores in the WAAM components has attracted considerable attention in recent years. Inter-layer rolling was introduced to eliminate micropores during the WAAM deposition of the Al−Cu6.3 and Al−Mg4.5 alloys. The distribution characteristics and individual morphology of micropores were revealed by the X-ray diffraction tomography. Key findings demonstrated that the number, volume, size, and roundness of micropores in rolled alloys decreased similarly with increasing loads, eventually achieving a density of over 99.9%. After the heat treatment, the homogeneous distribution of fine (around 5.3 μm) and spherical (0.70−0.74) micropores was realized in the 45 kN rolled alloys. All the evaluated indicators of micropores in the 45 kN rolled + heat treated alloys were superior to the post-deposition heat treated state. The evolution mechanisms include the reprecipitation of hydrogen pores, formation of vacant voids, and re-opening of unclosed pores. The hybrid technique of WAAM + rolling + heat treatment has great potential in promoting mechanical properties of WAAM alloys. The results will provide a theoretical guidance for the design of high-performance WAAM aluminum alloy components.

© 2019 The Authors. Published by Elsevier Ltd. This is an open access article under the CC BY-NC-ND license (http://creativecommons.org/licenses/by-nc-nd/4.0/).

1. Introduction

Additive manufacturing (AM) of aluminum alloy components has drawn broad attention from industrial customers in recent years. With the advantages of low cost and high deposition rate, wire + arc additive manufacturing (WAAM) has been recognized as

* Corresponding author.
E-mail address: baij@neuq.edu.cn (J. Bai).

https://doi.org/10.1016/j.matdes.2019.108288
0264-1275/© 2019 The Authors. Published by Elsevier Ltd. This is an open access article under the CC BY-NC-ND license (http://creativecommons.org/licenses/by-nc-nd/4.0/).

a promising AM technology in producing large-scale aluminum alloy structural parts [1]. However, the adverse effect of internal defects on mechanical properties has limited the application of WAAM aluminum alloys [2,3]. Micropores, as one of the most harmful defects, are normally detrimental to the fatigue, strength, and toughness of aluminum alloys [4]. This is because micropores can cause strain concentration yielding the load-bearing capacity and causing premature fracture [5]. Mayer et al. [6] reported micropores larger than approximately 50 μm generally act as the preferential crack initiation and propagation sites.

WAAM metallic materials such as titanium [7], steel [8], and Inconel 718 [9] can achieve a density of over 99.5% through optimization of process parameters. In comparison, aluminum alloys are one of the alloy systems more prone to porosity during fusion-based additive manufacturing [10]. A considerable number of pores with sizes from 10 to >100 μm are generally formed in the WAAM aluminum alloy [11]. Porosity is usually formed during solidification due to dissolved gas or volumetric shrinkage [12]. Hydrogen in aluminum alloys has been widely recognized as the dominant factor for the porosity formation during welding [13] or WAAM deposition [14]. The hydrogen solubility of the liquid aluminum, dropping down rapidly when temperature decreases, is almost 20 times larger than that of the solid [15]. By contrast, the solubility of hydrogen in the liquid and solid steel are about equal [5]. The insoluble hydrogen in aluminum is discharged from the solid-liquid interface into the surrounding liquid, causing hydrogen supersaturation and eventual micropores in the solidified metal. The sources of hydrogen include hydrocarbons (grease, oils, etc.) and moisture contaminants on surfaces of the wire and plate, or from the environment and shielding gases [10,13]. Gu et al. [14] reviewed hydrogen induced pores in aluminum are more difficult to be controlled for WAAM than welding. With a continuous wire-feeding during WAAM deposition, hydrocarbon contaminants on the wire surface from the wire drawing operation immediately convert into atomic hydrogen, which will be absorbed into the molten pool directly. The second cause of pore formation is incomplete feeding of solidification shrinkage, which is greatly dependent on the solidification range of metals. With increasing solidification range, liquid feeding becomes increasingly more difficult, unavoidably causing porosity during non-equilibrium solidification [12]. Moreover, Oliveira et al. [10] summarized porosity may also be caused by lack of fusion or evaporation of light elements.

When the aluminum alloys are subjected to high-temperature homogenization or solution treatment, the volume of secondary porosity usually becomes increasingly higher, accompanying with coalesce of small micropores [16]. The increase of micropores is due to various mechanisms including Ostwald ripening [17], hydrogen absorption [18], vacancy coalescence [16], or growth of existing pores and the nucleation of new pores in regions of incipient melted eutectic [19].

Porosity formation in aluminum, either hydrogen pores or volumetric shrinkage, has a close relationship with weld penetration, heat input, dendrite growth, grain shape/size, even shielding gas type and flow rate [10]. Comparatively higher heat input, greater penetration and coarser columnar grains prevent hydrogen escaping [20]. After exploring the influence of arc modes on the porosity formation in the WAAM Al−Cu6.3 alloy, Cong et al. [11] found the pulse advanced CMT mode performed better in controlling porosity due to the presence of refined equiaxed grains, lower heat input, and shallower dilution. They further eliminated porosity by lowering the heat input through optimization of current and travel speed [21]. The influence of travel speed by using tungsten inert gas (TIG) on the formation of porosity in the WAAM Al−Cu alloy was verified by Zhou et al. [22]. Besides, less porosity was formed in a lower proportion of electrode positive time cycle by using TIG. Ayarkwa et al. [23] attributed this to the finer grains, which reduce the tendency for pore formation due to the competition between heterogeneous nucleation of grains and pores. Wang et al. [24] found pulse frequency strongly affects the porosity of WAAM Al−Si5 alloy and attains the maximum in 50 HZ.

Nevertheless, pore defects in WAAM aluminum alloys are still difficult to be completely suppressed through parameter optimization. Horgar et al. [25] appealled for the development of new and high-quality feedstocks. This is because hydrogen pores are greatly influenced by the surface finish of wires, which could affect the hydrogen content and arc stability [14]. Ryan et al. [26] verified the quality and batch-to-batch variability in feedstock wire had a significant influence on the porosity size and distribution. Recently, researchers turned to develop hybrid WAAM technologies as universal methods to reduce or control porosity in aluminum alloys. Sun et al. [27] combined laser shock peening with WAAM producing Al−Cu alloys with higher density and finer grains. However, laser shock peening can only work on the part surface with a shallow penetration. Zhang et al. [28] reduced the porosity volume from 4.72% to 1.52% by vibrating the workpiece during the WAAM deposition. The added reciprocating force to the melt flow stirred the molten pool and benefited the overflow of internal bubbles, but micropores cannot be completely annihilated with increasing vibration acceleration. The application of ultrasonic wave [29], magnetic arc oscillation [30], or arc oscillation [31] are highly effective in promoting grain refinement and preventing pore defect, though they have not been used during additive manufacturing yet.

Toda et al. [32] and Chaijaruwanich et al. [33] separately reported the reduction, shrunk, and annihilation of micropores under cold rolling or 400 °C hot rolling in the Al−Mg alloy. Based on these findings, Gu et al. [34] applied local rolling to each and every layer during the deposition in developing a WAAM + inter-layer rolling hybrid manufacturing method. Except for the benefits in refining grain and improving mechanical properties, they found the size and number of micropores in the WAAM aluminum alloys were significantly decreased by using this method [35]. However, the results were obtained from the sample cross section by 2D inspection with optical microscopy. Uncertainty and inaccuracy can be generated because of the influence of residual abrasive powders from cutting and polishing during sample preparation. A micropore generally has disparate morphology from different section planes. The spatial distribution and morphology of micropores are difficult to reflect using 2D observation. In this study, X-ray diffraction tomography (XRT) was used to qualitatively and quantitatively explore the distribution and individual feature of micropores in WAAM aluminum alloys, thereby revealing their evolution behavior and mechanisms after inter-layer rolling and heat treatment. This study aims to propose an effective method in controlling micropores and providing a theoretical guidance for the design of high performance additively manufactured aluminum alloys.

2. Experimental methods

2.1. Materials and sample preparation

The commercial ER2319 (Al−Cu6.3) and ER5087 (Al−Mg4.5) wires with a diameter of 1.2 mm were used as raw materials. The nominal chemical composition of the wires is shown in Table 1. The deposited alloys are called Al−Cu6.3 and Al−Mg4.5 alloys, respectively. The 2219-T851 aluminum plate was used as the substrate and fixed by clamps. The surface of the substrate plate was washed in the alkaline water and dried in air, followed by mechanical cleaning and acetone degreasing. Single-pass multi-layers walls were bi-directionally deposited through a rolling rig integrated WAAM system [35]. A CMT Advanced 4000R power supply was

Table 1
Nominal chemical composition of the Al−Cu6.3 and Al−Mg4.5 aluminum alloy wires.

Alloys	Chemical composition (wt. %)									
	Cu	Mg	Mn	Ti	Zr	Cr	V	Si	Fe	Al
Al−Cu6.3	5.8−6.8	0.02	0.2−0.4	0.1−0.2	0.1−0.25	–	0.05−0.15	0.2	0.3	Bal.
Al−Mg4.5	0.05	4.5−5.2	0.7−1.1	0.15	0.1−0.2	0.05−0.25	–	0.25	0.4	Bal.

used as the heat source. Rolling loads were applied through a hydraulic cylinder to the roller (H13 steel), the diameter and width of which were 100 mm and 20 mm, respectively.

The pulse advanced CMT mode and the pulsed CMT mode were employed for the deposition of the Al−Cu6.3 and Al−Mg4.5 wall samples, respectively. According to the optimized parameters from pilot researches [11,36], deposition parameters in this study were set as constant for all the trails, the flow rate of shielding pure argon (99.99%) 25 L/min, arc torch and roller travel speed 0.6 m/min, wire feed speed 6 m/min, contact tip to workpiece distance 15 mm. The heat input of the deposition for each alloy was 126.7 J/mm and 177.9 J/mm. The initial rolling temperature was kept between 85 °C and 45 °C with an inter-layer cooling time of 2 min. As-deposited (0 kN), 15 kN, 30 kN and 45 kN rolled walls of each alloy were prepared. The total deformation rate of the rolled WAAM Al−Cu6.3 and Al−Mg4.5 alloys under each load was 13.9%, 30%, 44.2% and 14.1%, 31.3%, 45.4%. One as-deposited and one 45 kN rolled specimen of each alloy were heat treated under 535 °C for 90 min as the soaking time, followed by cold water quenching. The temperature range of 530−540 °C for aluminum alloys is the homogenization temperature [12,32,37], which is usually selected to lie in the single-phase aluminum solid solution region and is lower than the solidus line. The homogenization process in this study is mainly concerned with the reduction of micro-segregation and does not take into account the effect on porosity. The temperature of 535 °C is also adopted by the precipitation strengthened Al−Cu alloy for solution treatment [34].

Twelve specimens with six statuses, including as-deposited without rolling and heat treatment (AD), post-deposition heat treated (HT), 15 kN, 30 kN and 45 kN rolled (15 kN, 30 kN and 45 kN), 45 kN rolled + post-heat treated (45 kN+HT), were prepared for the Al−Cu6.3 and Al−Mg4.5 alloys. Samples for transmission electron microscopy (TEM) observation were prepared under a standard procedure and were twin-jet electro-polished at −30 °C and 15V with a solution of 30% nitric acid and 70% methanol. Microstructure images were taken by using JEM-2100F, JEOL. The dislocation density of each sample was estimated by the Dasharath's method from the X-ray diffraction [38]. The total hydrogen content of each specimen was measured by the inert gas fusion heat transfer method using the LECO ONH836 oxygen-nitrogen analyzer. Samples for XRT observation were sectioned from the central part of each wall along the longitudinal direction. All the samples were ground to a cuboid 0.8 mm × 0.8 mm in cross-section and 10 mm in length with grit SiC papers under a standard procedure, followed by ultrasonic wave washing in acetone at 30 °C to clean up the grease and abrasive powders.

2.2. Tomographic imaging and analysis

XRT tests were performed using the imaging line station B13W1 at the Shanghai Synchrotron Radiation Facility (SSRF). The synchrotron radiation X-ray imaging system consists of an X-ray source, a sample stage, a detector and a computer data processing system. The absorption contrasts imaging mode was used. The energy range of the synchrotron radiation is 8−72.5 keV with an accelerating voltage of 20 keV. Each specimen was positioned 150 mm from the camera. Visible wavelength photons were collected from a scintillator screen and focused onto a 2048 × 2048 element charge-coupled device (CCD). An objective lens of AA50 with a pixel size of 0.65 μm (voxel size 0.275 μm^3) was employed. The cross-sections with a height of 1331 μm were scanned in 180° around the loading axis with an increment of 0.125°. Eventually, 1440 radiographs with an exposure time of 1 s for each were ultimately captured on the CCD camera.

Phase recovery of the original contrast projection images was performed using the open source software P3 and P3B provided by SSRF. Slice images of each sample were reconstructed by the conventional filtered back projection algorithm. The grey value in each dataset was calibrated such that the linear absorption coefficient fell within an 8-bit grey scale ranging between 0 and 255. The commercial software Avizo was employed to segment micropores information based on 2048 slice images. All the micropores were eventually re-built and labeled as 3D images. The volume and surface area of each micropore were measured and calculated by the Marching Cubes method [39]. To suppress inaccuracies caused by image noise, micropores below 5 pixels or the equivalent diameter smaller than 3.25 μm, were not counted. Many micropores are caused by solidification cavities, exhibiting heteromorphic morphologies. Therefore, the concept of equivalent diameter d was introduced in Eq. (1) as the diameter of an ideal sphere having the same volume. Micropores sphericity S_p was defined in Eq. (2),

$$d = 2\sqrt[3]{3V/4\pi} \tag{1}$$

$$S_P = \sqrt[3]{36\pi V^2}/A \tag{2}$$

where V and A are the measured volume and surface area of a micropore.

2.3. Tensile test

The tensile tests were conducted in accordance with the standard ISO 6892-1 with a sample size as shown in Fig. 2 in Ref. [36]. Tensile test specimens, three in a set, were cut along the horizontal direction from each wall. An electromechanical universal testing machine Instron 5500R (30 kN) was employed for the tensile test at room temperature with an initial strain rate of 0.005 min^{-1}. Field emission scanning electron microscope (FE-SEM, PHILIPS-XL30E) was used to characterize the fracture surface morphology of tensile samples.

3. Results and discussion

3.1. Micropores morphology and distribution

Fig. 1 and Fig. 2 are 3D views of micropores with miscellaneous sizes and shapes in the as-deposited, rolled and heat treated WAAM Al−Cu6.3 and Al−Mg4.5 alloys. The concentration of micropores at the inter-layer boundary suggested that micropores tend to coalescent or float upward and to escape from the molten metal during solidification but may be hindered by dendritic arms and oxide films. Another possible reason was arisen from the arc and molten pool during subsequent deposition, which may cause an increase

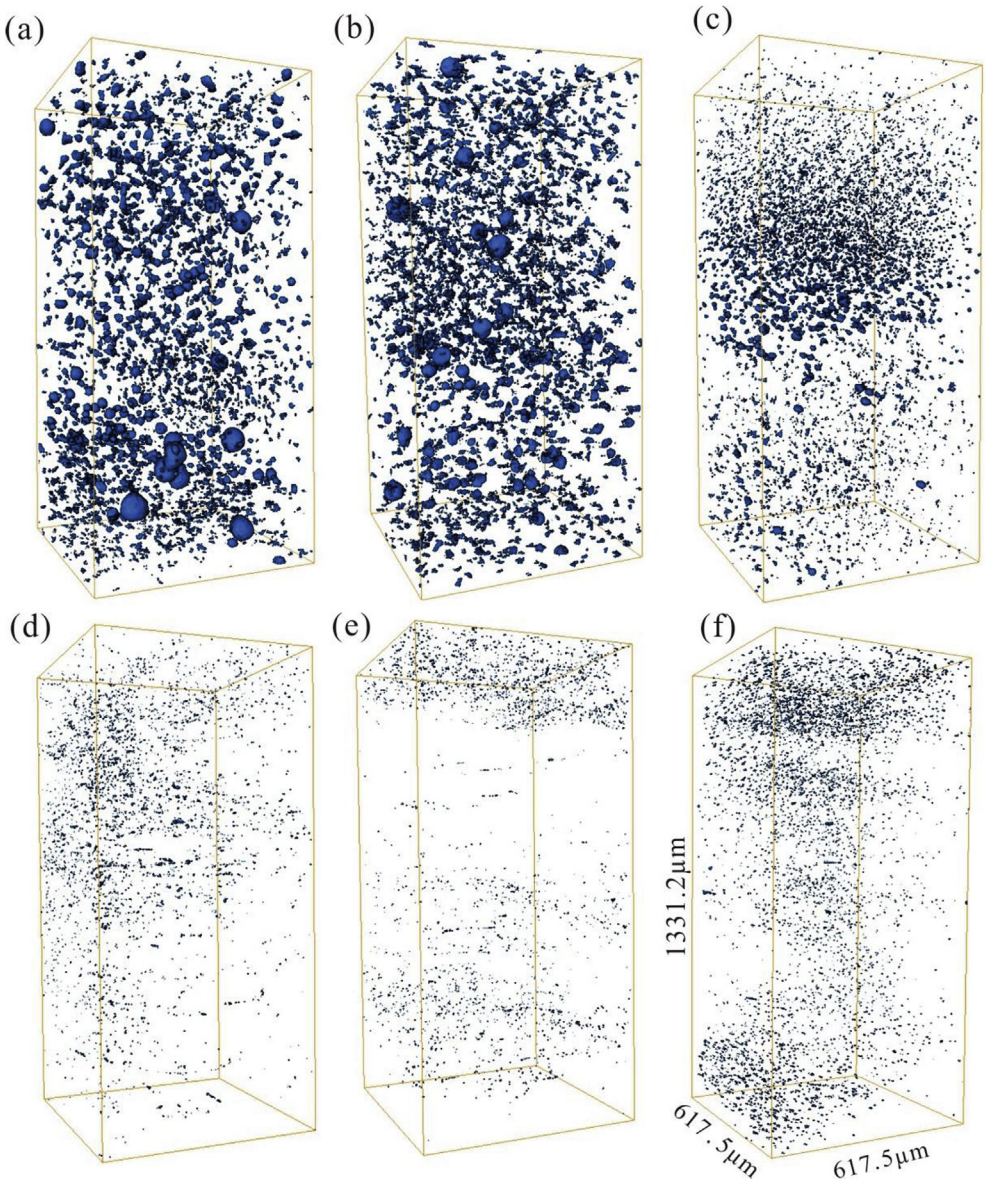

Fig. 1. 3D view of micropores in WAAM Al−Cu6.3 alloy; (a) as-deposited, (b) post-deposition heat treated, (c−e) 15 kN, 30 kN, 45 kN inter-layer rolled, and (f) 45 kN rolled + heat treated.

and growth of micropore in the local area. Eventually, large micropores were trapped at the top region of each layer.

The size and number of micropores in the rolled alloys sequentially decreased with increasing loads from 15 kN, 30 kN−45 kN. Residual micropores still clustered around the fusion line, suggesting that the original large micropores are hard to be annihilated unless the load keeps on rising. After heat treatment, a considerable number of fine micropores evenly distributed in the 45 kN rolled alloys. However, these re-initiated fine micropores were not observed by 2D observation [35] due to the resolution limit of the optical microscope.

Table 2 is a summary of the quantitative analysis of the density, volume, size, and roundness of micropores in WAAM alloys. After heat treatment, the number density increased nearly 2-fold whilst the volume fraction increased by 20% for the Al−Cu6.3 alloy. The micropores number in the Al−Mg4.5 alloy reduced by 7%. The 17% increase of micropores volume fraction of the Al−Mg4.5 alloy was similar to that of the Al−Cu6.3 alloy. The mean diameter of micropores after the heat treatment was reduced by 1.73 μm for the Al−Cu6.3 but increased by 0.29 μm for the Al−Mg4.5. The mean sphericity of micropores exhibited a decrease of 8% and an increase of 5% for each alloy. The number density, mean diameter and sphericity except the volume fraction of micropores behaved oppositely for the heat treated Al−Cu6.3 and Al−Mg4.5 alloys, suggesting different mechanisms may dominate the micropores evolution for these two alloys.

After the 15 kN inter-layer rolling, the number density and mean sphericity of micropores in the Al−Cu6.3 alloy exhibited an increase of 177% and 8%. There was a decrease of 26% and 5% for the Al−Mg4.5 alloy. The micropores volume fraction of the two alloys decreased at a similar level by 40% and 37%. The mean diameter of micropores in the Al−Cu6.3 alloy was 2.542 μm smaller whilst it was nearly unchanged in the Al−Mg4.5 alloy. The number density, volume fraction, and mean diameter of the micropores in the two 30 kN rolled alloys reduced similarly by 49% and 36%, 84% and 68%, 30% and 14% when compares with the 15 kN rolled status. The

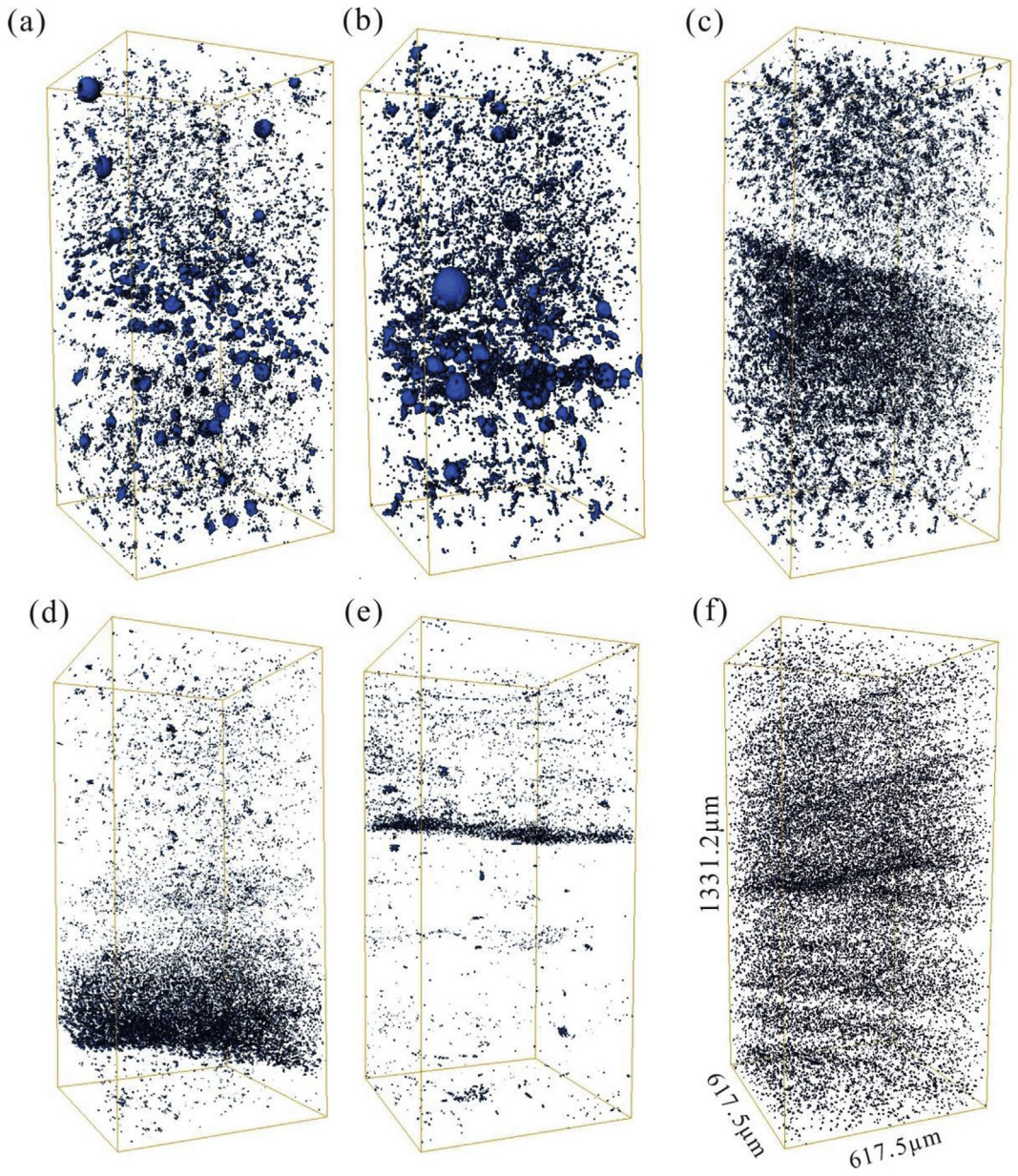

Fig. 2. 3D view of micropores in WAAM Al–Mg4.5 alloy; (a) as-deposited, (b) post-deposition heat treated, (c–e) 15 kN, 30 kN, 45 kN inter-layer rolled, and (f) 45 kN rolled + heat treated.

Table 2
Quantitative analysis of micropores in the WAAM Al–Cu6.3 and Al–Mg4.5 alloys under various conditions.

Alloys	Condition	Number density (10^3/mm^3)	Volume fraction (%)	Mean diameter (μm)	Mean sphericity
Al–Cu6.3	As-deposited	10.72	1.08	8.82	0.64
	Post-deposition heat treated	19.72	1.30	7.09	0.59
	15 kN inter-layer rolled	29.64	0.65	6.27	0.71
	30 kN inter-layer rolled	15.24	0.10	4.37	0.65
	45 kN inter-layer rolled	10.46	0.05	4.01	0.55
	45 kN rolled + heat treated	53.44	0.51	5.30	0.70
Al–Mg4.5	As-deposited	56.10	1.06	5.38	0.69
	Post-deposition heat treated	52.24	1.24	5.68	0.72
	15 kN inter-layer rolled	41.76	0.67	5.50	0.60
	30 kN inter-layer rolled	26.80	0.22	4.71	0.70
	45 kN inter-layer rolled	13.63	0.07	4.13	0.50
	45 kN rolled + heat treated	80.50	0.74	5.31	0.74

mean sphericity of micropores in the Al–Cu6.3 alloy decreased by 9% but it increased by 9% for the Al–Mg4.5. The abnormal increase of mean sphericity after rolling may be attributed to the increasing number of small micropores, which will be further discussed in Section 3.3. When the load raised to 45 kN, a reduction of 31% and 49%, 55% and 66%, 8% and 12%, 15% and 28% were observed for the

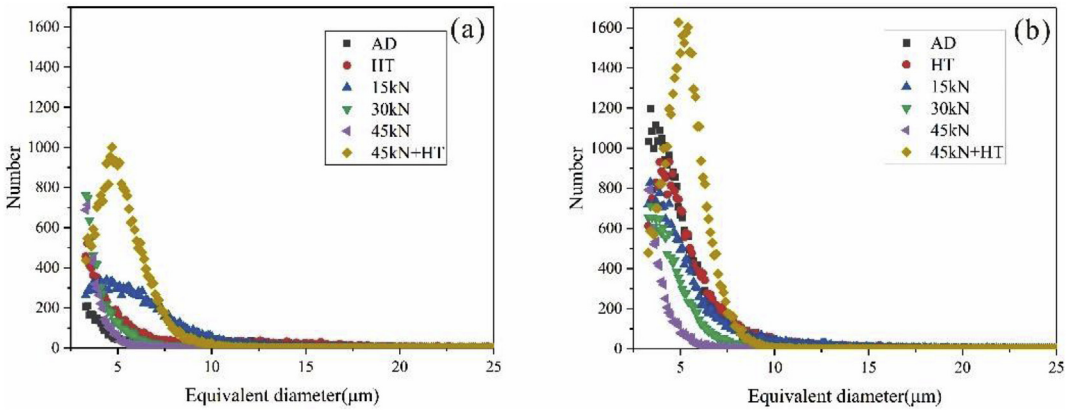

Fig. 3. Micropore numbers distribution as a function of equivalent diameter in WAAM alloys within a volume of 0.5×10^9 μm^3; (a) Al−Cu6.3 and (b) Al−Mg4.5 aluminum alloys.

micropores number density, volume fraction, mean diameter, and sphericity of both alloys. Although the number density of fine micropores in both the 45 kN rolled alloys was still above 10×10^3 per mm^3, a high density of over 99.9% was achieved by using this hybrid WAAM-rolling technique.

Micropores in both the 45 kN rolled alloys behaved similarly after the heat treatment. A homogeneous scatter of fine and near-round micropores in the WAAM alloys were realized eventually by the hybrid technique of WAAM + inter-layer rolling + heat treatment (WAAM-RHT). The number density of micropores in the Al−Cu6.3 and Al−Mg4.5 alloys sharply increased nearly 5-fold and 6-fold, respectively. The volume fraction was 9−10 times enlarged. The mean diameter was around 5.3 μm with an increase of nearly 30% in both alloys.

Fig. 3 is the micropores number scattering plot as a function of the equivalent diameter with an interval of 0.1 μm. Most micropores of the two alloys concentrated within a region below 10 μm under various conditions. After the heat treatment, the number of micropores within all sizes increased in the unrolled Al−Cu6.3 alloy. Particularly, the number of small micropores ranging between 3.25 μm and 10.25 μm increased significantly by 124.5%. By contrast, the number of micropores within this size, especially smaller than 6.25 μm, was reduced by about 8% in the Al−Mg4.5 alloy. After the inter-layer rolling, the peak value moved toward the left under increasing loads. The micropores number of the rolled Al−Mg4.5 alloy cut down sequentially from the as-deposited status as shown in Fig. 3(b). However, an abnormal growth of number of small micropores (3.25−10.25 μm) was found in the 15 kN rolled Al−Cu6.3 alloy, which is still larger than the as-deposited state until 45 kN. The number of micropores larger than 10.25 μm in the 15 kN rolled Al−Cu6.3 alloy dropped off by 54% and nearly disappeared when the load reached 30 kN and 45 kN. In comparison, micropores larger than 10.25 μm in the Al−Mg4.5 alloy reduced by nearly 12% and 92% under 15 kN and 30 kN, respectively. Large micropores were not detected under 45 kN. The average diameter of micropores in the two 45 kN rolled alloys concentrated below 5 μm, which takes up 90% and 93% of the total volume of micropores in the two alloys, respectively. A sharp growth of the micropores number for both the 45 kN rolled alloys was evident when they were heat treated. The maximum value of number was around 5.3 μm for both alloys. Micropores ranging between 3.25 and 7 μm in the Al−Mg4.5 alloy was larger than that of the Al−Cu6.3 with a factor of 1.6.

Fig. 4 plots the number distribution of micropores by sorting their sphericity at an interval of 0.02. After the heat treatment, the number of micropores with small sphericity, less than 0.5, increased by 204% in the Al−Cu6.3 alloy. Micropores having larger sphericity increased by only 6%. By contrast, the number of micropores within corresponding sphericity reduced by 21% but increased by 12% for the heat treated Al−Mg4.5 alloy. After rolling, the number of micropores in both alloys became less for the entire sphericity range whilst the peak value of each curve moved to the left with increasing loads, indicating that micropores were flattened to be oval after rolling. One distinct exception for the Al−Cu6.3 alloy was that more micropores with larger sphericity emerged under 15 kN. Subsequently, many micropores with sphericity from 0.6 to 0.85, mostly around 0.7, were generated after the heat treatment in both the 45 kN rolled alloys.

Fig. 5 plots the sphericity distribution as a function of the equivalent diameter. For the Al−Mg4.5 alloy, the scattering of sphericity after heat treatment was not changed, while micropores in the Al−Cu6.3 alloy became more dispersed. The lower left shift of the scatter figure indicated the formation of fine aspheric micropores in the heat treated alloy. This result is in accordance with the great increase of micropore numbers as listed in Table 2. After the rolling, the overall distribution became narrower with increasing loads moving toward the lower left corner except the 15 kN rolled Al−Cu6.3 alloy. When the two 45 kN rolled samples were heat treated, fine micropores with larger sphericity concentrated within a narrow region. Micropores scattering at the lower right corner of this region have bulged from the ones that were not completely closed during the 45 kN rolling.

3.2. *Micropores formation during deposition and evolution after heat treatment*

Individual round micropores in Fig. 6(a and b) and chain-like cavities (or microcracks) in Fig. 6(c and d), formed by different mechanisms, were found in the as-deposited WAAM alloys. Comparatively, most of the individual micropores in the Al−Mg4.5 alloy exhibited a smoother surface as shown in Fig. 6(b). Individual hydrogen micropores are generally formed due to the precipitation of supersaturated hydrogen, which heterogeneously nucleates on the second phases, grain boundaries, or inclusions. By contrast, the cavity defect is commonly caused by solidification shrinkage or insufficient liquid feeding to the interfaces between phases or dendritic arms [35]. Toda et al. [17] found angular micropores in a crystallographic orientation relationship under 550 °C over 90 h due to the tendency in reducing surface energy. They assumed that an octahedral micropore is prone to form by surrounded eight {111} planes in achieving energetical stability. The formation of this oriented pore is not likely for the WAAM alloy in this study due to its rapid solidification rate and less high-temperature exposure period.

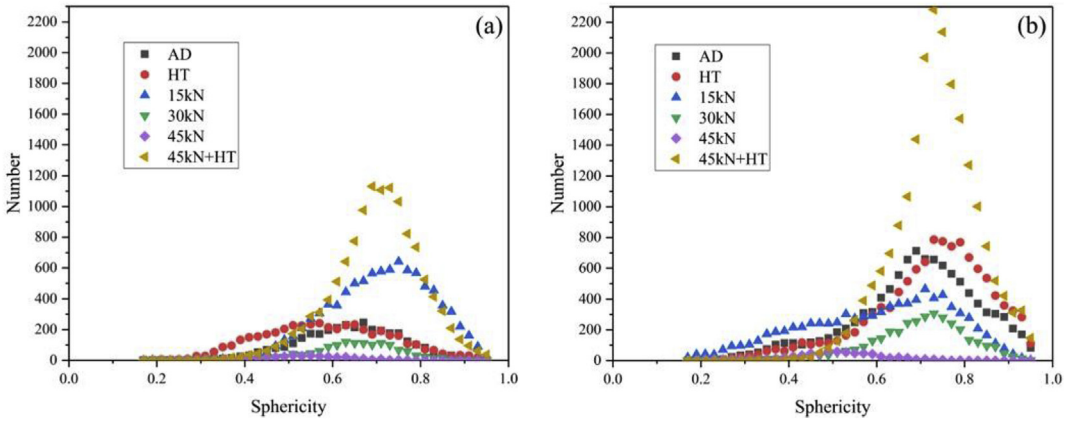

Fig. 4. Micropores number distribution as a function of sphericity in WAAM alloys within a volume of $0.5 \times 10^9\ \mu m^3$; (a) Al–Cu6.3 and (b) Al–Mg4.5 aluminum alloys.

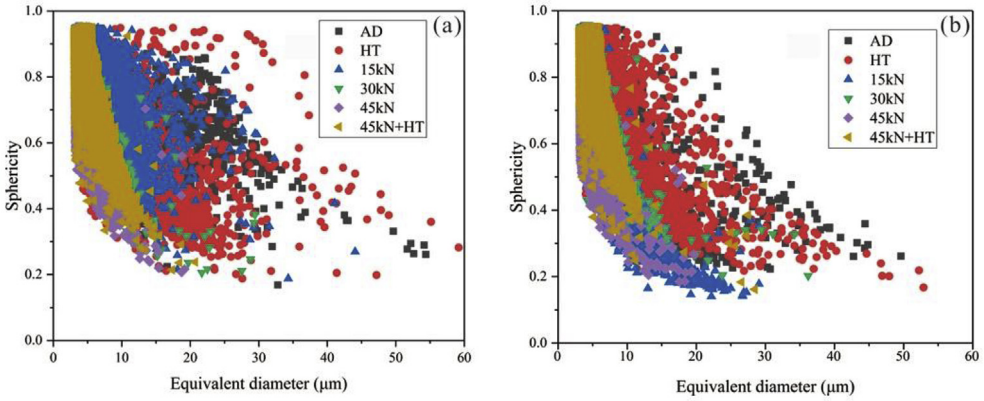

Fig. 5. Scatter plot of micropores sphericity as a function of equivalent diameter in WAAM alloys; (a) Al–Cu6.3 and (b) Al–Mg4.5 aluminum alloys.

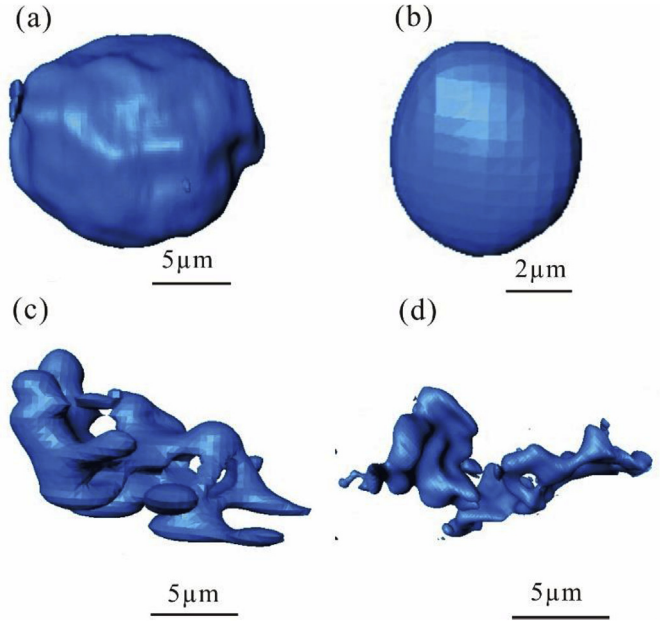

Fig. 6. Typical morphology of micropores in as-deposited WAAM alloys; (a, c) Al–Cu6.3 and (b, d) Al–Mg4.5, where (a, b) are individual micropores, (c, d) are solidification cavities.

The distribution of micropores with various morphology in the WAAM alloys is exhibited in Fig. 7. Micropores were mainly cavity-like in Fig. 7(a) of the as-deposited Al–Cu6.3 alloys whilst small and near-round micropores homogeneously distributed in the Al–Mg4.5 alloy (Fig. 7(c)). After the heat treatment, more irregular micropores were found in the Al–Cu6.3 as shown in Fig. 7(b). Micropores in the Al–Mg4.5 alloy in Fig. 7(d) became coarsening and less in quantitative terms. The number density (ρ_P) of micropores in the heat treated Al–Mg4.5 alloy in Table 3 was decreased by 7% in spite of a constant total content of hydrogen (M_H) comparing with the Al–Cu6.3 alloy. Together with the small increase of mean diameter ($\bar{d}$) of micropores, it suggested that the growth of micropores in the Al–Mg4.5 alloy is likely dominated by Ostwald ripening. Micropores in the rapidly solidified WAAM alloy are always unstable if the total interfacial free energy γ is not a minimum. It is known that γ increases as the radius of curvature decreases, establishing an energy gradient between micropores in various sizes. Due to the Gibbs-Thomson effect [12], the average radius (r_{ave}) increases with time as defined by Eq. (3) [40] accompanying with total number decrease,

$$r_{ave}^3 - r_0^3 = kt \tag{3}$$

where r_0 is the mean radius at time t = 0. The growth coefficient k is proportional to the diffusion coefficient D and γ. According to the Arrhenius equation of diffusion, D increases exponentially with temperature. The rate of micropores coarsening grows rapidly with increasing temperature. Vacancy and hydrogen diffuse under high temperature in the direction of the local largest pores away from the smallest, so that the small ones shrink and disappear while large ones grow.

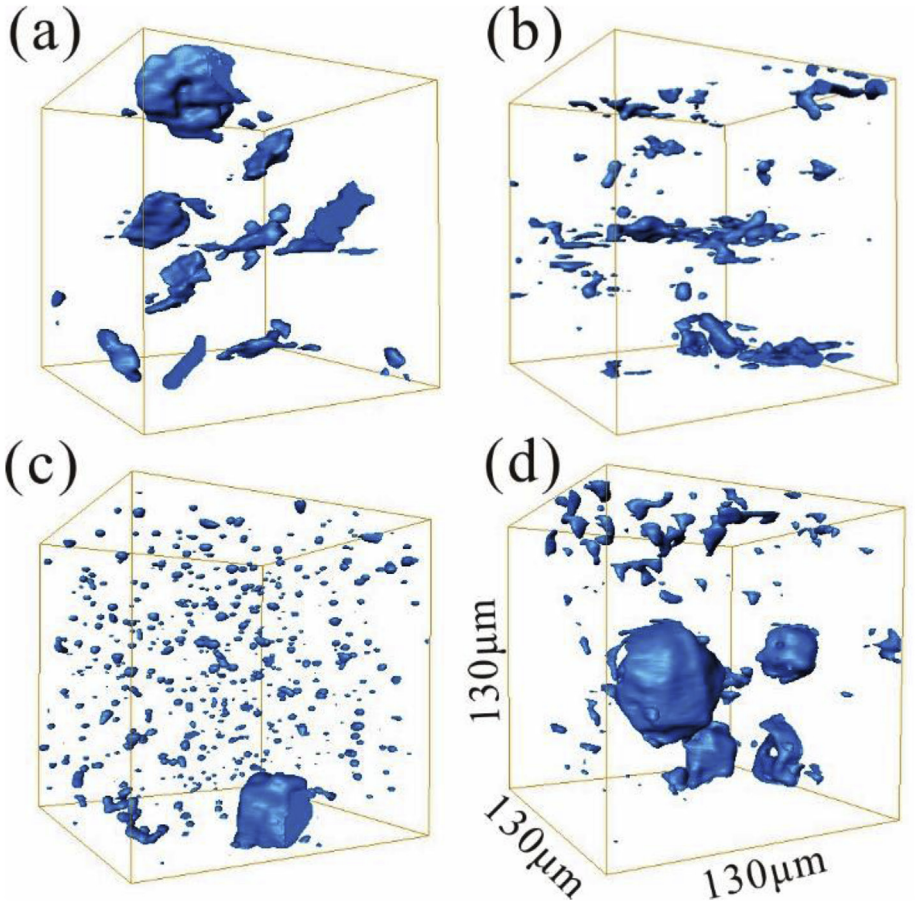

Fig. 7. Distribution and morphology of micropores in WAAM alloys; (a, b) Al−Cu6.3 and (c, d) Al−Mg4.5, where (a, c) are as-deposited and (b, d) are post-deposition heat treated.

Table 3
The measured total hydrogen content, micropores number density, and mean diameter of the as-deposited and heat treated WAAM alloys.

Alloys	Condition	Total hydrogen content M_H (cm^3/100 g Al)	Micropores number density ρ_P ($10^3/mm^3$)	Mean diameter $\overline{d}$ (μm)
Al− Cu6.3	as-deposited	14.76	10.72	8.82
	post-deposition heat treated	14.89	19.72	7.09
Al− Mg4.5	as-deposited	26.61	56.10	5.38
	post-deposition heat treated	27.69	52.24	5.68

Comparatively, the 84% increase in ρ_P of the Al−Cu6.3 alloy together with its increase of volume fraction but a decrease in mean diameter and sphericity, indicated that Ostwald ripening is not the predominant factor of the micropores evolution for this alloy. The subsidiary relationship between micropores and phase particles in the Al−Cu6.3 alloys, at an interval of one-voxel, is revealed in Fig. 8. The eutectics of α-Al+ Al_2Cu are primary second phases [3]. Fig. 8(a) is the 2D grey value of a virtual slice, where black and white were micropores and phase particles embedding in the grey aluminum matrix. Due to the Fresnel diffraction [41], light and dark stripes appear at interfaces between each micropore and matrix, phase particle and matrix, or micropore and particle. The presence of stripes may result in a significant separation between phase particles and micropores in segmenting virtual slice images, as shown in Fig. 8(b). The spatial micropores generally attached to neighboring second phases as reconstructed in Fig. 8(c). The interface indicates that heterogeneous nucleation occurs on pre-existing particles [17], which normally scatter at the inter-dendritic region acting as nuclei for hydrogen precipitation during solidification. Hydrogen pores will expand as dendritic arms growing. Solidification cavities, which were recognized as microcracks, may also form due to insufficient liquid feeding at the inter-dendritic region under high cooling rates [42].

According to calculation, 61% of the micropores attached to phase particles in the Al−Mg4.5 alloys (Fig. 9). This ratio was 83% and 76% for the as-deposited and heat-treated Al−Cu6.3 alloy. Fig. 10 is the 3D distribution of second phase particles. The volume fraction of second phase particles was over 22% in the as-deposited Al−Cu6.3 alloy. As shown in Fig. 10(a), micropores usually grow along with the network of eutectic particles resulting in many large micropores with low sphericity in this alloy. After the heat treatment, eutectic phases were significantly reduced and became increasingly granular as shown in Fig. 10(b). Fewer second phase particles were found in the as-deposited Al−Mg4.5 alloy (Fig. 10(c)). They were unobtrusively changed after the heat treatment whilst the micropores became larger and less (Fig. 10(d)).

As shown in Fig. 11, 81% of the reticulated second phases were dissolved in the Al−Cu6.3 alloy after heat treatment whilst it was 18% of the Al−Mg4.5 alloy, in spite of a similar rise of micropore volume fraction in the two heat treated alloys. It is reasonable to

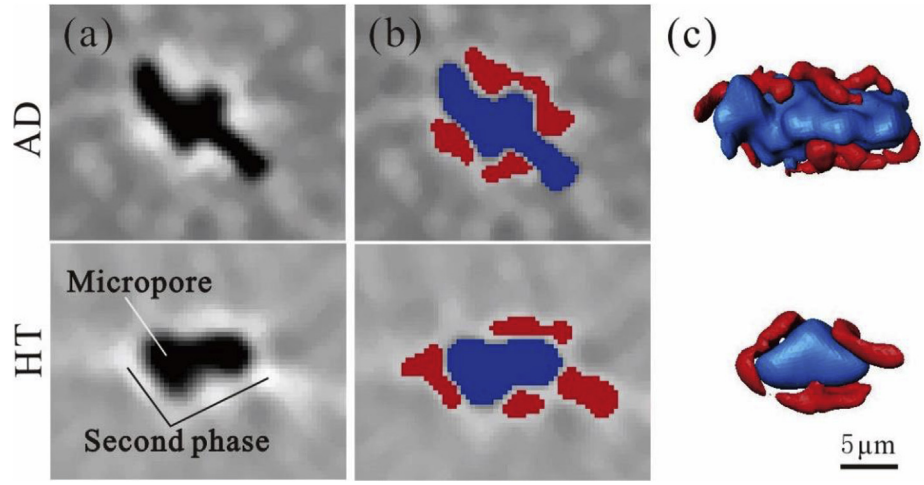

Fig. 8. Dependence of micropores (blue) on phase particles (red) of the as-deposited and heat-treated WAAM Al–Cu6.3 alloy; (a) 2D slice of a reconstructed volume, (b) segmented micropore and phase particle, (c) 3D view.

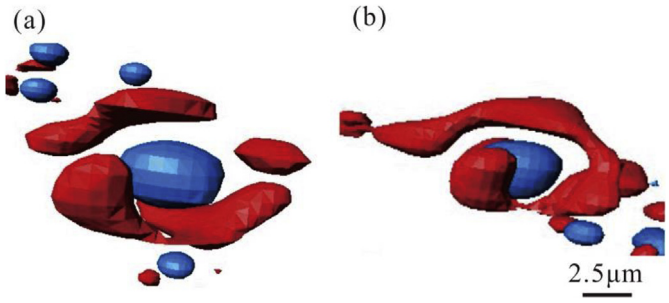

Fig. 9. Dependence of micropores (blue) on phase particles (red) of the WAAM Al–Mg4.5 alloy; (a) as-deposited and (b) post-deposition heat treated.

assume that the vacant voids caused by the dissolution of second phase particles in the Al–Cu6.3 alloy lead to the increased number of irregular micropores after the heat treatment. Given the small size of the original eutectics (generally less than 15 μm), fine pores were considerably increased in the heat treated alloy (Fig. 3) in spite of the growth of pre-existing pores. This also explains the 8% decrease of mean sphericity and the 20% decrease of mean diameter of micropores in the heat treated Al–Cu6.3 alloy. Anyalebechi and Hogarth [19] also attributed the formation of porosity to solidification cavities in regions of incipient melted eutectics in investigating the effect of heat treatments on aluminum 2014. Therefore, the complex variation of micropores of the heat-treated Al–Cu6.3 alloy is mainly controlled by phase particles dissolution, companying with micropores growth and hydrogen micropores precipitation.

3.3. Micropores evolution after rolling and heat treatment

The typical morphology of the incompletely closed individual micropores in the two WAAM alloys from each rolling step is shown in Fig. 12. Small micropores can be closed under rolling whilst larger individual micropores are flattened. The solidification cavities may be gradually broken into several smaller ones and spheroidized as shown in Fig. 12(d), which may explain the abnormal increase number of small micropores in the 15 kN rolled Al–Cu6.3 alloy given its great proportion of chain-like cavities. Toda et al. [37] also found that micropores in casting aluminum alloys break up one by one during the cold-working. When the force reached 45 kN, most micropores larger than 5 μm were closed leaving a proportion of 0.05%–0.07% of fine micropores in both alloys. When the 45 kN rolled samples were heat treated, smooth and spherical fine micropores re-initiated as shown in Fig. 12(e).

As analyzed in Fig. 11, the contents of second phase particles in the rolled Al–Cu6.3 and Al–Mg4.5 alloys stayed steadily around 22% and 5%, respectively. However, the crushed particles became more homogeneously distributed under increasing loads as shown in Fig. 13 of the Al–Cu6.3 alloy whilst the micropores were stretched and elongated (Fig. 14). After the heat treatment, the volume fraction of phase particles of the 45 kN rolled Al–Cu6.3 alloy was significantly reduced to nearly 5% in Fig. 13(d). The fine diameter of the undissolved near-spherical particles was around 5 μm. The retained or reprecipitated micropores scattered neighboring to the residual particles or in-between as observed from the 3D dependence relations of them in Fig. 14(c). The evolution of phase particles and micropores was likely similar to that of the rolled Al–Mg4.5 alloy. The volume fraction of the particles after the heat treatment was around 5% as well. However, particle coarsening was observed in Fig. 13(h), which is different from that of the Al–Cu6.3 alloy.

In conclusion, three possible factors may contribute to the increase of micropores quantity, volume, size and roundness during the heat treatment for the rolled WAAM alloys. First, high-temperature exposure may cause the reprecipitation of secondary porosity due to the supersaturated content of hydrogen. When hydrogen atoms are desorbed under high-temperatures from dislocations release or interfaces migration, micropores will heterogeneously nucleate on particles and grow spatially. Second, the residual vacant voids may be formed especially in the Al–Cu6.3 alloy from the dissolving phase particles during heat treatment. Last, nearly 0.1% volume of micropores is not completely closed under 45 kN rolling. They will be re-opened and spheroidized during the subsequent heat treatment.

3.4. The role of hydrogen

As shown in Table 4, the measured hydrogen content M_H was 14.76 cm^3 and 26.61 cm^3 per 100 g as-deposited WAAM Al–Cu6.3 and Al–Mg4.5 alloys. This value is 5 orders of magnitude larger than the equilibrium solid solubility of hydrogen, which is 3.9×10^{-4} cm^3 per 100g Al at room temperature [43]. Smith and Scully [44] concluded that the preferred trapping sites of hydrogen in aluminum alloys are crystal defects like solute atoms, lattice gaps, dislocations, precipitates and high-angle grain boundaries. This is

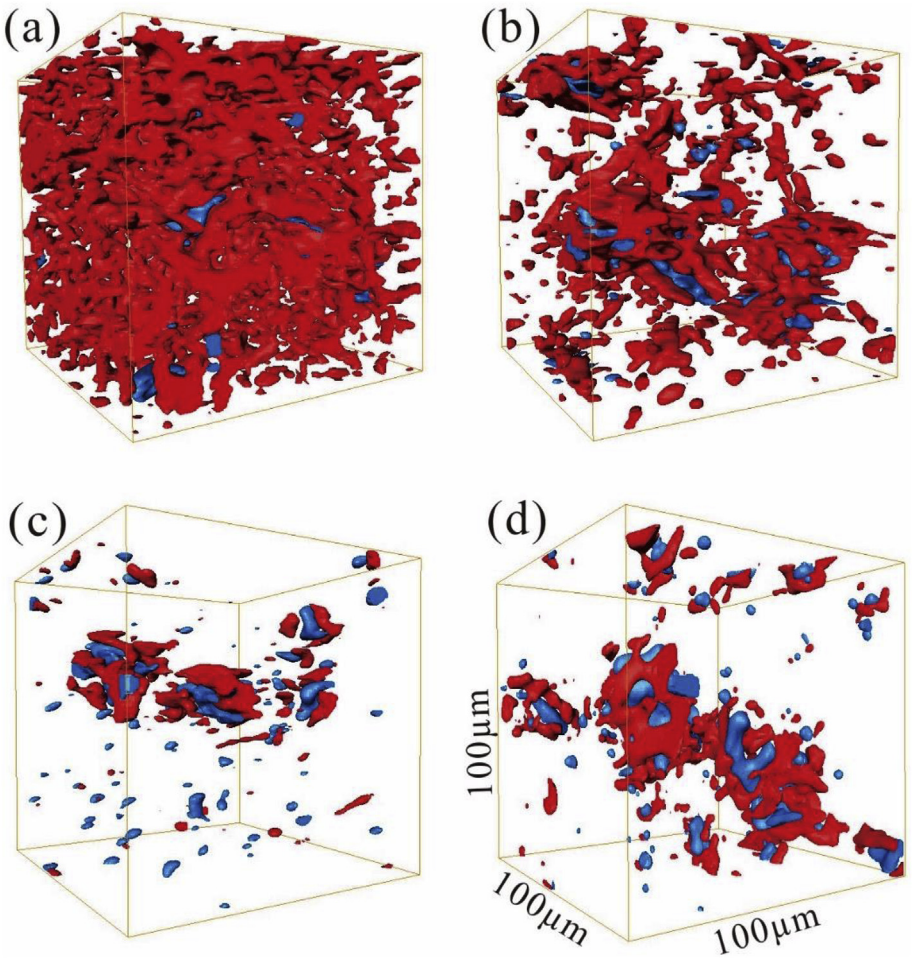

Fig. 10. Distribution of second phases (red) and micropores (blue) in WAAM alloys; (a,b) Al–Cu6.3 and (c,d) Al–Mg4.5, where (a,c) as-deposited and (b,d) post-deposition heat treated.

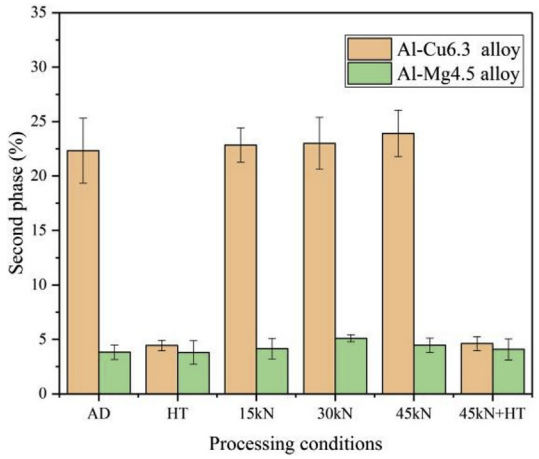

Fig. 11. Volume fraction of second phase particles in WAAM Al–Cu6.3 and Al–Mg4.5 alloys.

likely for the WAAM alloy given its vast heterogeneous nucleation sites for the supersaturated atomic hydrogen. Out-law et al. [45] claimed that more than 99% of the hydrogen is trapped in the micropores of the pure aluminum, which is lacking of hydrogen trapping sites. Previous studies suggested that hydrogen may exist as the molecule gas in the individual micropores or precipitate in the body defects like cracks or voids. Toda et al. [17] proposed a reasonable assumption that micropores may approach thermal equilibrium. The surface tension (γ) is balanced by the opposite gas pressure (P) inside a micropore as $4\gamma/d = P$. d is the micropore diameter. Combining with the ideal gas law, the hydrogen content C^H_{Pore} (mol) trapped in all the micropores was obtained by summing the hydrogen content in each pore as Eq. (4):

$$C^H_{Pore} = \sum \frac{2\pi\gamma d_i^2}{3RT} \tag{4}$$

where d_i is the diameter of the ith micropore, R is the gas constant and T is temperature. Surface tension γ is assumed to be 1.16 Nm^{-1} for the (111) face [17]. The equivalent content of hydrogen in micropores was represented by M^H_{Pore}, which is the equivalent hydrogen gas at 0 °C and 1 atm per 100 g alloy. The fraction of hydrogen in micropores F^H_{Pore} was calculated by M^H_{Pore}/M_H. The M^H_{Pore} of the as-deposited Al–Mg4.5 alloy in Table 4 was 1.8 times larger than that of the Al–Cu6.3 alloy. The larger content of hydrogen explains why a considerably higher amount of smaller (around 4 μm) and rounder (over 0.7) individual hydrogen micropores were found in the as-deposited Al–Mg4.5 alloy. Under this original situation, the fraction of hydrogen trapped in micropores (F^H_{Pore}) was 7.9% for both the as-deposited alloys.

The storage hydrogen was not lost under heat treatment and inter-layer rolling or a combination of them. After the heat treatment, M_H of both alloys was slightly increased. M^H_{Pore} of the Al–Cu6.3 and the Al–Mg4.5 alloys increased by 26% and 5%,

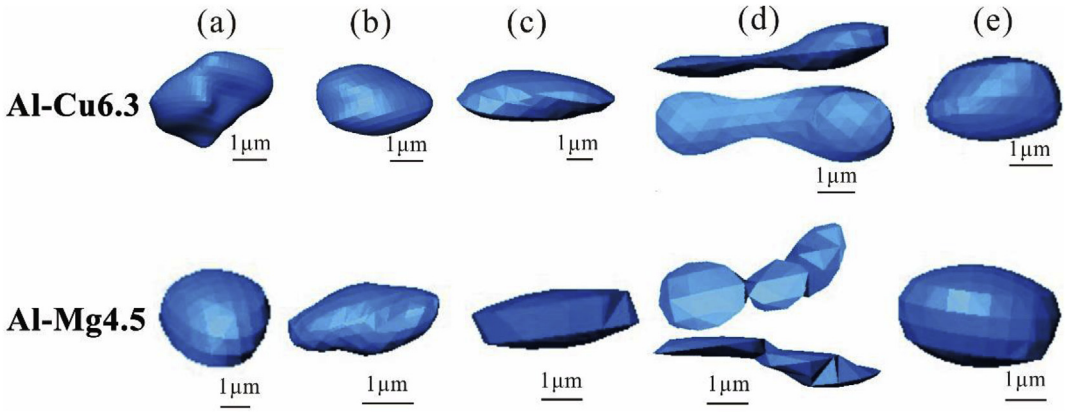

Fig. 12. Evolution of a single micropore in WAAM Al–Cu6.3 and Al–Mg4.5 alloys; (a) as-deposited, (b–d) 15 kN, 30 kN, and 45 kN inter-layer rolled, (e) 45 kN rolled + heat treated.

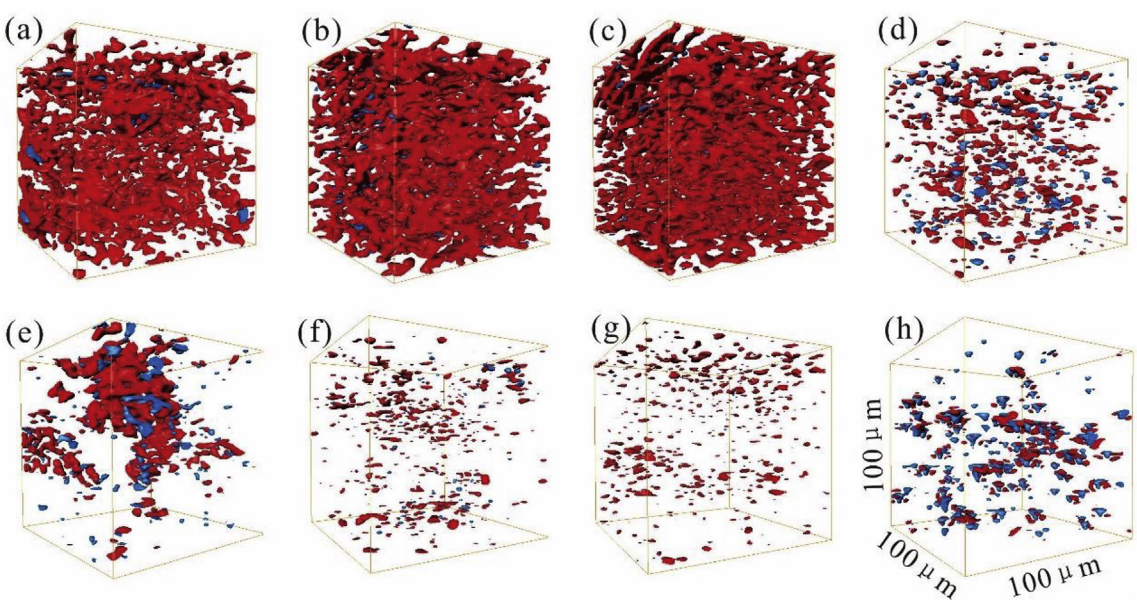

Fig. 13. Distribution of second phases (red) and micropores (blue) in WAAM alloys; (a–d) Al–Cu6.3 and (e–h) Al–Mg4.5, where (a,e), (b,f), (c,g) are 15 kN, 30 kN, 45 kN inter-layer rolled and (d,h) is 45 kN rolled + heat treated.

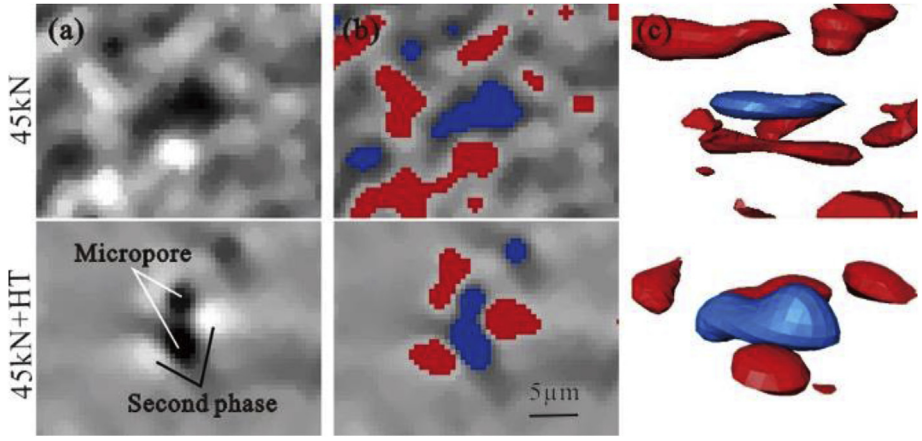

Fig. 14. Dependence of micropores (blue) on phase particles (red) in 45 kN rolled and heat-treated WAAM Al–Cu6.3 alloy; (a) 2D slice of a reconstructed volume, (b) segmented micropore and phase particle, (c) 3D view.

respectively. By contrast, F^{H}_{Pore} of the Al–Cu6.3 increased by 24% but it was nearly unchanged for the Al–Mg4.5. This difference may be originated from the great gap between the content of second phase particles and the distinguishing phase transformation mechanisms of the two alloys. The enhancement of F^{H}_{Pore} of the Al–Cu6.3 alloy was caused by the precipitated hydrogen pores, which came from

Table 4
The measured hydrogen content, calculated hydrogen content in micropores, fraction of hydrogen in micropores and the dislocation density of the WAAM alloys.

Alloys	Condition	Total H_2 content M_H (cm^3/100 g Al)	H_2 content in micropores M^H_{Pore}(cm^3/100 g Al)	Fraction of H_2 in micropores F^H_{Pore} (%)	Dislocation density ($10^{13}/m^2$)
Al−Cu6.3	As-deposited	14.76	1.16	7.9	8.2
	Post-deposition heat treated	14.89	1.46	9.8	10.4
	15 kN rolled	20.47	1.33	6.5	17.6
	30 kN rolled	37.31	0.32	0.9	36.5
	45 kN rolled	22.97	0.18	0.8	44.1
	45 kN rolled + heat treated	20.79	1.55	7.5	12.7
Al−Mg4.5	As-deposited	26.61	2.10	7.9	9.5
	Post-deposition heat treated	27.69	2.21	8.0	12.8
	15 kN inter-layer rolled	31.19	1.57	5.0	19.3
	30 kN inter-layer rolled	42.21	0.68	1.6	44.4
	45 kN inter-layer rolled	28.19	0.26	1.0	50.2
	45 kN rolled + heat treated	29.12	2.47	8.5	11.6

the hydrogen directly discharged from the dissolving phase particles. Su et al. [46] found the nucleation and growth speed of hydrogen micropores is faster on spherical and small particles than other sites. The hydrogen status of the 5087 alloy was not changed under heat treatment.

M_H of the rolled Al−Cu6.3 and Al−Mg4.5 alloys increased by 39%, 153%, 56% and 17%, 59%, 6% with increasing loads, reaching a summit in both alloys under 30 kN. Hydrogen may be absorbed by the potential "pipes effect", which states the metal surface is connected by dislocations generated during cold rolling [32]. This is possible for the rolled WAAM alloy as well. A considerably increasing density of dislocation was developed in the WAAM-RHT alloys as shown in Fig. 15. The cyclic heat input during deposition may magnify the rates of absorption and diffusion of the atmosphere hydrogen, which may be trapped at the vast storage sites of the rolled alloys. Under 45 kN, the absorption and release of hydrogen through the "pipes" may approach a dynamic balance, leading to a sharp decrease of the total hydrogen content. The volume of phase particles in the Al−Cu6.3 alloy was nearly 6 times larger than the Al−Mg4.5 alloy. The micro-voids formed by particles crushing will provide more channels for hydrogen absorption. This may explain the higher increase of hydrogen content of the Al−Cu6.3 alloy.

M^H_{Pore} and F^H_{Pore} of both alloys gradually reduced with increasing loads. F^H_{Pore} of the two 45 kN rolled alloys ranged between 0.8% and 1%, indicating that 99%−99.2% of hydrogen was trapped in the solid crystal. Toda et al. [32] pointed out that when the equilibrium state of micropores is wrecked by compression, molecular hydrogen can be dissociated to atoms, which will dissolve into the matrix and trapped at tremendous storage sites like dislocations or vacancies. The great hydrogen storage capability of these defects was verified by several studies [17,44,47]. The vacancies generated in this study may migrate out of the crystal due to the thermal activation of the subsequent heat input. Therefore, the influence of vacancy on hydrogen absorption was not taken into consideration. Although the cyclic heat can release the accumulated local stress to some extent as well, a large number of dislocations were still found in the WAAM alloys as shown in Fig. 15. This occurred in the Al−Mg4.5 alloy as well. The content of hydrogen absorbed in the matrix in Table 4 was almost linearly grown with the increasing dislocation density under incremental rolling loads.

After the heat treatment, the total hydrogen content M_H of the 45 kN rolled samples was nearly unchanged. However, M^H_{Pore} and F^H_{Pore} of both rolled+heat treated alloys were dramatically increased by about 10 times closing to the level of the as-deposited state. Given the decrease of the total volume V_{Pore} of micropores, if we take each as-deposited state as a reference and use M^H_{Pore}/V_{Pore} to represent the fraction of hydrogen micropores from the total, the content of the hydrogen micropores in the Al−Cu6.3 and Al−Mg4.5 alloys increased by 183% and 68% by using the WAAM-RHT method.

3.5. Effect of micropores and hydrogen on mechanical properties

The tensile properties of the as-deposited, rolled, and heat treated WAAM Al−Cu6.3 and Al−Mg4.5 alloys have been investigated by our group [34,36]. The stress-strain curves are shown in Fig. 16. The ultimate tensile strength (UTS) of the as-deposited Al−Cu6.3 and Al−Mg4.5 alloys was 260 MPa and 290 MPa, respectively. Micropores were arrowed in yellow on the fracture surface from SEM observation in Figs. 17(a) and 18(a). Although the coarse dimples indicated a ductile fracture for the as-deposited alloys, micropores may act as crack initiation sites as arrowed in Fig. 17(a) of the Al−Cu6.3 alloy. The elongation of larger pores along the tensile force direction, initiating crack propagation and finally resulting in fractured surface, has been revealed by Ma et al. [48] using the in-situ tensile test with the X-ray microscope. In comparison, pore induced cracks under tensile was not obvious on the fracture surface of the as-deposited Al−Mg4.5 alloy (Fig. 18(a)), which may be the reason for the higher strain rate of this alloy.

Under growing 15-30-45 kN rolling loads, the UTS increased by 3.8%, 10.7%, and 20.6% for the Al−Cu6.3 alloy, and 3.4%, 10%, and 18.2% for the Al−Mg4.5 alloy, with a consequential decrease in the elongation. The strengthening effect of dynamic strain aging revealed by the serrated patterns was found in the as-deposited

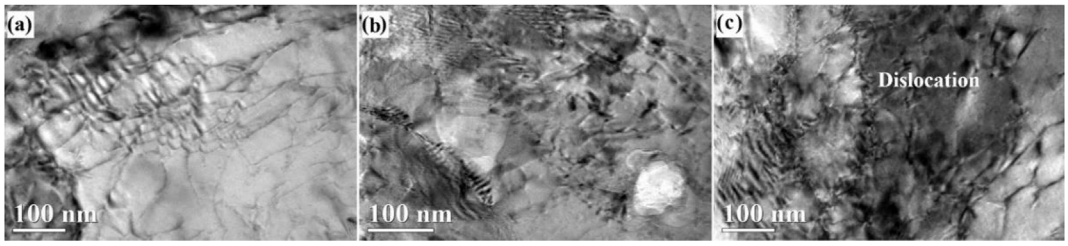

Fig. 15. TEM images of inter-layer rolled WAAM Al−Cu6.3 alloy; (a) 15 kN, (b) 30 kN, and (c) 45 kN rolled.

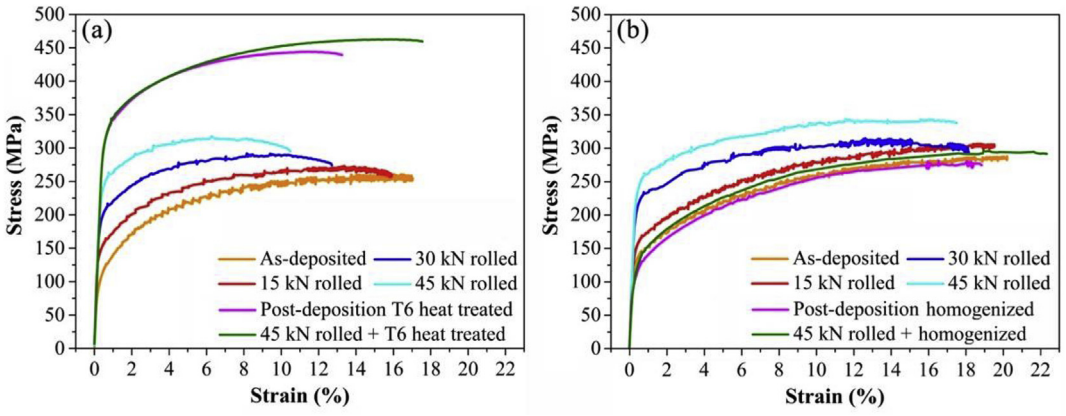

Fig. 16. Stress-strain curves of WAAM alloys; (a) Al–Cu6.3 and (b) Al–Mg4.5.

and rolled alloys, and became less apparent with increasing loads. The dimples became finer and more evenly distributed on the fracture surface of 45 kN rolled alloys in Figs. 17(c) and 18(c). The formation of a high density of dislocation and sub-grain, and the reduction of grain size were conventionally thought responsible for the strength improvement [34,36]. The shrink of micropores which were normally ignored may be one significant factor in affecting mechanical properties as well. As discussed in Section 3.1 and 3.3, most of the micropores were suppressed during rolling, which prompts the strength of the part as an integrity. However, the incomplete annihilation of micropores may yield mechanical properties. This is because tip-concentrated stresses of squashed micropores can accelerate crack fracture and lower the plasticity. The influence of the pore morphology on the stress intensity was verified in both experiments and calculation by pilot authors [49].

To reach the final application state with peak precipitation strengthening, artificial aging (T6) was conducted on the Al–Cu6.3 alloy under 175 °C for 3 h, after the 535 °C heat treatment and water quenching. The micropores changes very slightly after aging due to its low temperature. The homogenization status of the Al–Mg4.5 alloy was kept at 535 °C because it is a non-heat treatable alloy. With shallower and finer dimples on the fracture surface in Fig. 17(b) and (d), the UTS of the T6 heat treated Al–Cu6.3 alloy reached 450 MPa due to precipitation strengthening with the presence of nano-sized metastable precipitates [34]. The UTS of the homogenized Al–Mg4.5 alloy stayed around 280–295 MPa, which is similar to the as-deposited level because of the slightly changed phase volume as stated in Figs. 10 and 13. After heat treatment, the elongation of the 45 kN rolled material was 23% and 19% higher than the as-deposited Al–Cu6.3 and Al–Mg4.5 alloys, respectively. Except for the refinement of grains [34], the reduction of large pores (crack initiation site) as shown in Figs. 17(d) and 18(d), and the homogeneous distribution of phase particles in Fig. 13(d) and (h) may attribute to the remarkable improvement of the plasticity of WAAM-RHT alloys. The beneficial effect of homogeneous fine pores has been verified by Toda et al. [50] from 4D observation that the growth of micropores instead of the particle rupture dominates the ductile fracture of aluminum alloys.

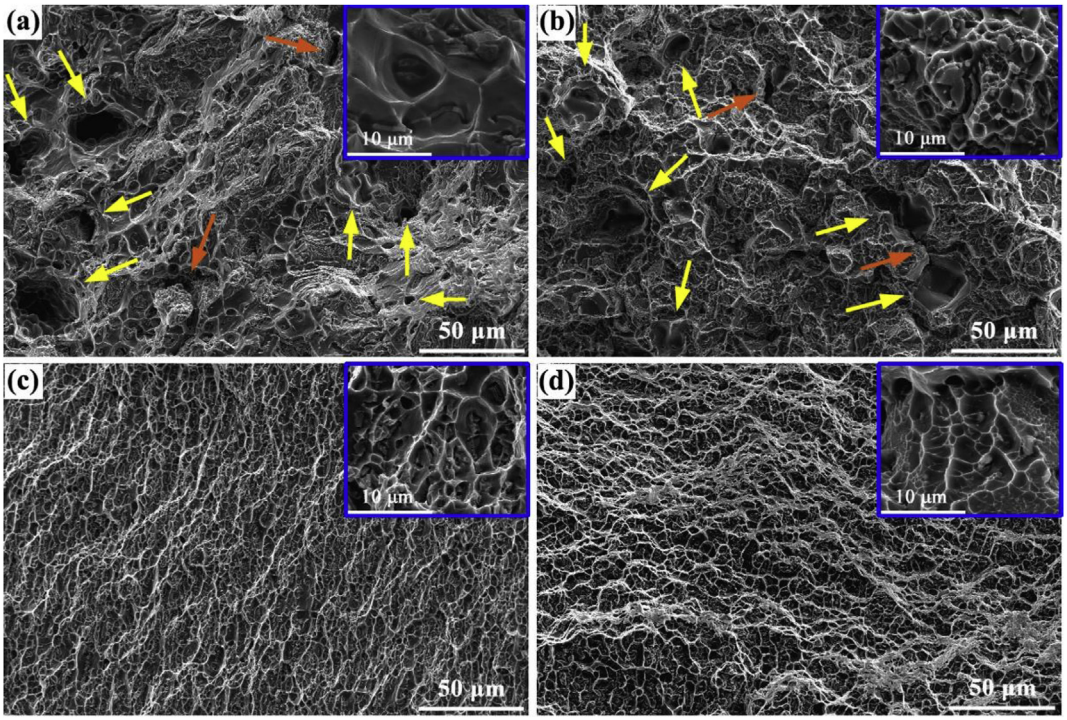

Fig. 17. SEM fractographic morphology of WAAM Al–Cu6.3 alloys; (a) as-deposited, (b) post-deposition T6 heat treated, (c) 45 kN rolled, and (d) 45 kN rolled + T6 heat treated.

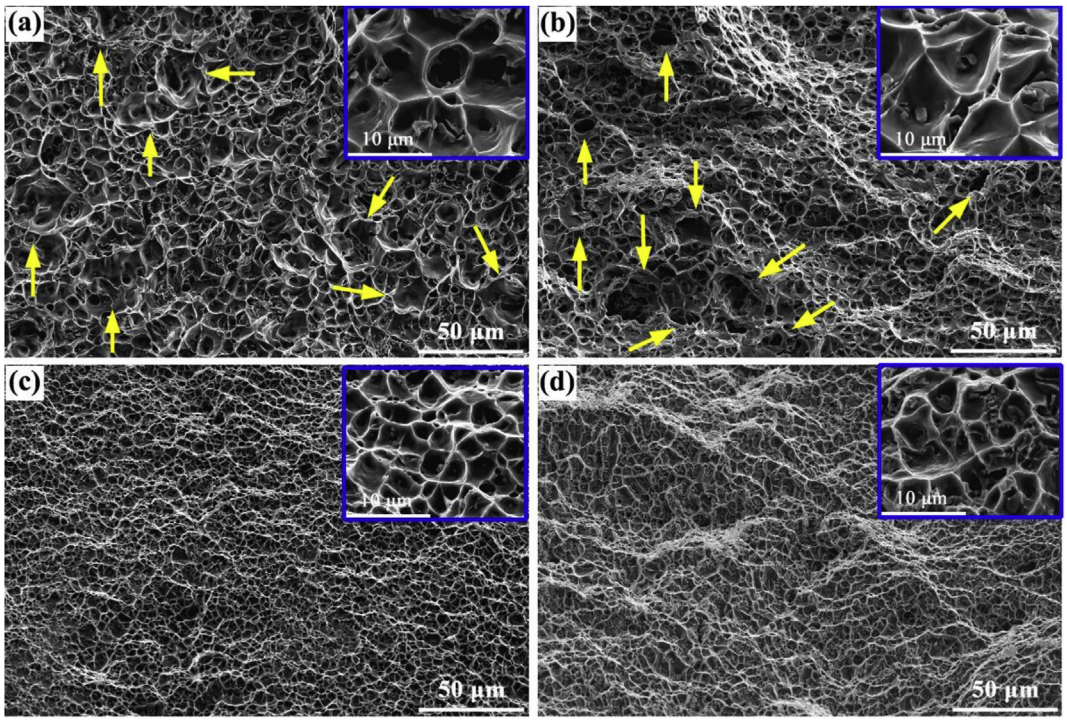

Fig. 18. SEM fractographic morphology of WAAM Al–Mg4.5 alloys; (a) as-deposited, (b) post-deposition homogenized, (c) 45 kN rolled, and (d) 45 kN rolled + homogenized.

The strength and elongation of the WAAM-RHT Al–Cu6.3 alloy are relatively higher than that of the wrought alloy with the same composition [34]. With a similar spatial distribution of strengthening phase particles, the total number, volume, and sphericity of micropores in the WAAM-RHT alloy are close to or higher than that of the conventional wrought alloy. For example, the micropores number density of the WAAM-RHT alloy is close to the upper limit in the conventional alloys, which is about 8000 to 70,000 per mm^3 [50]. The micropores volume fraction of 0.51–0.74% of the WAAM-RHT alloy is larger than the commercial alloy, which was reported as 0.25% [51]. The increase of the strength and plasticity of the WAAM alloy seems like contradictory to the results from Talbot et al. [43], who claimed that the mechanical properties of aluminum alloys can be seriously weakened when the porosity volume ranges between 0.5% and 1%.

However, the mean sphericity of 0.70–0.74 for the WAAM-RHT alloys is similar to that of the cold rolled Al–Mg alloy from Toda et al. [32], who claimed the mean sphericity of re-initiated micropores was 0.74 after annealing. The average diameter of the homogeneously distributed near-spherical micropores in both WAAM-RHT alloys is around 5 μm, which is smaller than the general size of 8–13 μm in wrought alloys. Besides, the supersaturated hydrogen content reaches over 20 cm^3 per 100 g WAAM alloys due to its rapid cooling rate. By contrast, it ranges only 0.11–0.60 cm^3 per 100 g wrought alloys. The influence of dispersed fine micropores and supersaturated hydrogen on the mechanical properties of WAAM alloys are still unclear. Great efforts should be made to understand the complex interaction among the micropores, second phases, and matrix and to reveal the influence of the binding energy of the metastable hydrogen storage structures on the mechanical properties.

4. Conclusion

The influence of inter-layer rolling and heat treatment on the evolution of micropores in the WAAM Al–Cu6.3 and Al–Mg4.5 alloys was studied. Behaviors of growth, closure, annihilation, and re-initiation of micropores were observed by using the XRT method. The number of fine (around 4 μm) individual hydrogen micropores with sphericity over 0.7 in the as-deposited Al–Mg4.5 alloy was about 5 times larger than that of the Al–Cu6.3. After the heat treatment, the number, size, and sphericity except the volume of micropores in the two alloys behaved oppositely. The micropores growth of the Al–Mg4.5 alloy was primarily dominated by Ostwald ripening. By contrast, the decrease of the size and sphericity of micropores in the Al–Cu6.3 alloy may be caused by the formation of vacant voids from the dissolving phase particles. After the inter-layer rolling, the number, volume, size, and roundness of micropores in both alloys decreased similarly with increasing rolling loads, except that an increasing number of small (3.25–10.25 μm) and round micropores existed in the 15 kN rolled Al–Cu6.3 alloy and the 30 kN rolled Al–Mg4.5 alloy. This abnormal increase of small pores was caused by the crushing of chain-like cavities. A high density of over 99.9% can be achieved under the 45 kN rolling eventually. The atomic hydrogen may be trapped at the considerably increased dislocations. After the heat treatment, fine (around 5.3 μm) and spherical (0.70–0.74) micropores homogeneously scattered of in the two 45 kN rolled WAAM alloys. However, the number and total volume of micropores were 5–6 times and 9–10 times enlarged. The reprecipitation of hydrogen pores, the formation of vacant voids, and re-opening of unclosed pores are the main factors. The estimated content of hydrogen micropores in the WAAM Al–Cu6.3 and Al–Mg4.5 alloys increased by 183% and 68%, respectively. The dispersed fine micropores and the supersaturated hydrogen may positively affect the mechanical properties of the WAAM aluminum alloys.

Acknowledgements

This work was supported by the China Postdoctoral Science Foundation (2017M621103) and Natural Science Foundation of Hebei Province (E2019203364). Thanks also go to Shanghai Synchrotron Radiation Facility in China for their help in testing with the beamline BL13W1.

References

[1] S.W. Williams, F. Martina, A.C. Addison, J.L. Ding, G. Pardal, P.A. Colegrove, Wire + arc additive manufacturing, Mater. Sci. Technol. 32 (2015) 641–647.
[2] B.T. Wu, Z.X. Pan, D.H. Ding, D. Cuiuri, H.J. Li, J. Xu, J. Norrish, A review of the wire arc additive manufacturing of metals: properties, defects and quality improvement, J. Manuf. Process. 35 (2018) 127–139.
[3] X. Fang, L.J. Zhang, H. Li, C. Li, K. Huang, B.H. Lu, Microstructure evolution and mechanical behavior of 2219 aluminum alloys additively fabricated by the cold metal transfer process, Materials 11 (2018) 812.
[4] Y.B. Zhang, J.H. Xu, T.G. Zhai, Distributions of pore size and fatigue weak link strength in an A713 sand cast aluminum alloy, Mater. Sci. Eng. A 527 (2010) 3639–3644.
[5] R.J. Fruehan, P.N. Anyalebechi, Gases in Metals, ASM Handbook, 2008, pp. 64–73.
[6] H. Mayer, M. Papakyriacou, B. Zettl, S.E. Stanzl-Tschegg, Influence of porosity on the fatigue limit of die cast magnesium and aluminum alloys, Int. J. Fatigue 25 (2003) 245–256.
[7] H. Attar, M.J. Bermingham, S. Ehtemam-Haghighi, A. Dehghan-Manshadi, D. Kent, M.S. Dargusch, Evaluation of the mechanical and wear properties of titanium produced by three different additive manufacturing methods for biomedical application, Mater. Sci. Eng. A 760 (2019) 339–345.
[8] T.A. Rodrigues, V. Duarte, J.A. Avila, T.G. Santos, R.M. Miranda, J.P. Oliveira, Wire and arc additive manufacturing of HSLA steel: effect of thermal cycles on microstructure and mechanical properties, Addit, Man (Lond.) 27 (2019) 440–450.
[9] C.E. Seow, H.E. Coules, G. Wu, R.H.U. Khan, X. Xu, S. Williams, Wire + Arc Additively Manufactured Inconel 718: effect of post-deposition heat treatments on microstructure and tensile properties, Mater. Des. 183 (2019) 108157.
[10] J.P. Oliveira, T.G. Santos, R.M. Miranda, Revisiting fundamental welding concepts to improve additive manufacturing: from theory to practice, Prog. Mater. Sci. (2019) 100590, doi.org/10.1016/j.pmatsci.2019.100590.
[11] B. Cong, J. Ding, S.W. Williams, Effect of arc mode in cold metal transfer process on porosity of additively manufactured Al-6.3% Cu alloy, Int. J. Adv. Manuf. Technol. 76 (2015) 1593–1606.
[12] A. Chaijaruwanich, P.D. Lee, R.J. Dashwood, Y.M. Youssef, H. Nagaumi, Evolution of pore morphology and distribution during the homogenization of direct chill cast Al-Mg alloys, Acta Mater. 55 (2007) 285–293.
[13] J.H. Devletian, W. Wood, Factors Affecting Porosity in Aluminum Welds-A Review, Welding Research Council, Bulletin, 1983, pp. 1–18.
[14] J.L. Gu, J.L. Ding, B.Q. Cong, J. Bai, H.M. Gu, S.W. Williams, Y.C. Zhai, The influence of wire properties on the quality and performance of wire+arc additive manufactured aluminium parts, Adv. Mater. Res. 1081 (2014) 210–214.
[15] A.P. Boeira, I.L. Ferreira, A. Garcia, Alloy composition and metal/mold heat transfer efficiency affecting inverse segregation and porosity of as-cast Al-Cu alloys, Mater. Des. 30 (2009) 2090–2098.
[16] D.E.J. Talbot, D.A. Granger, Secondary hydrogen porosity in aluminum, J. Inst. Met. 92 (1963) 290–297.
[17] H. Toda, T. Hidaka, M. Kobayashi, K. Uesugi, A. Takeuchi, K. Horikawa, Growth behavior of hydrogen micropores in aluminum alloys during high-temperature exposure, Acta Mater. 57 (2009) 2277–2290.
[18] M.F. Jordan, G.D. Denyer, A.N. Turner, Porosity in high-strength semi-continuously cast aluminium-copper-magnesium alloy ingots, J. Inst. Met. 91 (1962), 48.
[19] P.N. Anyalebechi, J. Hogarth, Effect of supereutectic homogenization on incidence of porosity in aluminum alloy 2014 ingot, Metall. Mater. Trans. B 25 (1994) 111–122.
[20] K.S. Derekar, A review of wire arc additive manufacturing and advances in wire arc additive manufacturing of aluminium, Mater. Sci. Technol. 34 (2018) 1–22.
[21] B.Q. Cong, R.J. Ouyang, B.J. Qi, J.L. Ding, Influence of cold metal transfer process and its heat input on weld bead geometry and porosity of aluminum-copper alloy welds, Rare Metal Mater. Eng. 45 (2016) 606–611.
[22] Y.H. Zhou, X. Lin, N. Kang, W.D. Huang, J. Wang, Z.N. Wang, Influence of travel speed on microstructure and mechanical properties of wire + arc additively manufactured 2219 aluminum alloy, J. Mater. Sci. Technol. (2019) doi.org/10.1016/j.jmst.2019.06.016.
[23] K.F. Ayarkwa, S.W. Williams, J. Ding, Assessing the effect of TIG alternating current time cycle on aluminium wire+arc additive manufacture, Addit. Manuf. 18 (2017) 186–193.
[24] D.H. Wang, J.P. Lu, S.Y. Tang, L. Yu, H.L. Fan, L. Ji, C.M. Liu, Reducing porosity and refining grains for arc additive manufacturing aluminum alloy by adjusting arc pulse frequency and current, Materials 11 (2018) 1344.
[25] A. Horgar, H. Fostervoll, B. Nyhus, X. Ren, M. Eriksson, O.M. Akselsen, Additive manufacturing using WAAM with AA5183 wire, J. Mater. Process. Technol. 259 (2018) 68–74.
[26] E. Ryan, T.G. Sabin, J. Watts, M. Whiting, The influence of build parameters and wire batch on porosity of wire and arc additive manufactured aluminium alloy 2319, J. Mater. Process. Technol. 262 (2018) 577–584.
[27] R. Sun, L. Li, Y. Zhu, W. Guo, P. Peng, B. Cong, J. Sun, Z. Che, B. Li, C. Guo, L. Liu, Microstructure, residual stress and tensile properties control of wire-arc additive manufactured 2319 aluminum alloy with laser shock peening, J. Alloy. Comp. 747 (2018) 255–265.
[28] C. Zhang, M. Gao, X.Y. Zeng, Workpiece vibration augmented wire arc additive manufacturing of high strength aluminum alloy, J. Mater. Process. Technol. 271 (2019) 85–92.
[29] W.L. Dai, Effects of high-intensity ultrasonic-wave emission on the weldability of aluminum alloy 7075-T6, Mater. Lett. 57 (2003) 2447–2454.
[30] J. Zhou, H.L. Tsai, Effects of electromagnetic force on melt flow and porosity prevention in pulsed laser keyhole welding, Int. J. Heat Mass Transf. 50 (2007) 2217–2235.
[31] N.S. Biradar, R. Raman, Grain refinement in Al-Mg-Si alloy TIG welds using transverse mechanical arc oscillation, J. Mater. Eng. Perform. 21 (2012) 2495–2502.
[32] H. Toda, K. Minami, K. Koyama, K. Ichitani, M. Kobayashi, K. Uesugi, Y. Suzuki, Healing behavior of preexisting hydrogen micropores in aluminum alloys during plastic deformation, Acta Mater. 57 (2009) 4391–4403.
[33] A. Chaijaruwanich, R.J. Dashwood, P.D. Lee, H. Nagaumi, Pore evolution in a direct chill cast Al-6 wt.% Mg alloy during hot rolling, Acta Mater. 54 (2006) 5185–5194.
[34] J.L. Gu, J.L. Ding, S.W. Williams, H.M. Gu, J. Bai, Y.C. Zhai, P.H. Ma, The strengthening effect of inter-layer cold working and post-deposition heat treatment on the additively manufactured Al-6.3Cu alloy, Mater. Sci. Eng. A 651 (2016) 18–26.
[35] J.L. Gu, J.L. Ding, S.W. Williams, H.M. Gu, P.H. Ma, Y.C. Zhai, The effect of inter-layer cold working and post-deposition heat treatment on porosity in additively manufactured aluminum alloys, J. Mater. Process. Technol. 230 (2016) 26–34.
[36] J.L. Gu, X.S. Wang, J. Bai, J.L. Ding, S.W. Williams, Y.C. Zhai, K. Liu, Deformation microstructures and strengthening mechanisms for the wire+arc additively manufactured Al-Mg4.5Mn alloy with inter-layer rolling, Mater. Sci. Eng. A 712 (2018) 292–301.
[37] H. Toda, T. Yamaguchi, M. Nakazawa, Y. Aoki, K. Uesugi, Y. Suzuki, M. Kobayashi, Four-dimensional annihilation behaviors of micro pores during surface cold working, Mater. Trans. 51 (2010) 1288–1295.
[38] S.M. Dasharath, S. Mula, Microstructural evolution and mechanical properties of low SFE Cu-Al alloys processed by cryorolling followed by short-annealing, Mater. Des. 99 (2016) 552–564.
[39] H. Cline, Marching cubes: a high resolution 3D surface construction algorithm, ACM SIGGRAPH Comput. Graph. 21 (1987) 163–169.
[40] D.A. Porter, K.E. Easterling, M.Y. Sherif, Phase Transformations in Metals and Alloys, third ed., CRC Press, 2008, p. 310.
[41] P. Cloetens, M. Pateyron-Salome, J.Y. Buffiere, G. Peix, J. Baruchel, F. Peyrin, M. Schlenker, Observation of microstructure and damage in materials by phase sensitive radiography and tomography, J. Appl. Phys. 81 (1997) 5878–5886.
[42] J.L. Gu, J. Bai, J.L. Ding, S. Williams, L.M. Zhai, K. Liu, Design and cracking susceptibility of additively manufactured Al-Cu-Mg alloys with tandem wires and pulsed arc, J. Mater. Process. Technol. 262 (2018) 210–220.
[43] D.E.J. Talbot, Effects of hydrogen in aluminium, magnesium, copper, and their alloys, Int. Metall. Rev. 20 (1975) 166–184.
[44] S.W. Smith, J.R. Scully, The identification of hydrogen trapping states in an Al-Li-Cu-Zr alloy using thermal desorption spectroscopy, Metall. Mater. Trans. A 31 (2000) 179–193.
[45] R.A. Outlaw, D.T. Peterson, F.A. Schmidt, Hydrogen partitioning in pure cast aluminum as determined by dynamic evolution rate measurements, Metall. Trans. A 12 (1981) 1809–1816.
[46] H. Su, S. Bhuiyan, H. Toda, K. Uesugi, A. Takeuchi, Y. Watanabe, Influence of intermetallic particles on the initiation and growth behavior of hydrogen micropores during high-temperature exposure in Al-Zn-Mg-Cu aluminum alloys, Scr. Mater. 135 (2017) 19–23.
[47] W.G. Wolfer, M.I. Baskes, Interstitial solute trapping by edge dislocations, Acta Metall. 33 (1985) 2005–2011.
[48] T.J. Ma, J.G. Ge, Y. Chen, T.N. Jin, Y.P. Lei, Observation of in-situ tensile wire-arc additively manufactured 205A aluminum part: 3D pore characteristics and microstructural evolution, Mater. Lett. 237 (2019) 266–269.
[49] R. Hidalgo, J.A. Esnaola, I. Llavori, M. Larrañaga, I. Hurtado, N. Herrero-Dorca, Fatigue life estimation of cast aluminium alloys considering the effect of porosity on initiation and propagation phases, Int. J. Fatigue 125 (2019) 468–478.
[50] H. Toda, H. Oogo, K. Horikawa, K. Uesugi, A. Takeuchi, Y. Suzuki, M. Nakazawa, Y. Aoki, M. Kobayashi, The true origin of ductile fracture in aluminum alloys, Metall. Mater. Trans. A 45 (2014) 765–776.
[51] H. Toda, I. Sinclair, J.Y. Buffière, E. Maire, K.H. Khor, P. Gregson, T. Kobayashi, A 3D measurement procedure for internal local crack driving forces via synchrotron X-ray microtomography, Acta Mater. 52 (2004) 1305–1317.

https://dspace.org/

Micropore evolution in additively manufactured aluminum alloys under heat treatment and inter-layer rolling

Gu, Jianglong; Yang, Shouliang; Gao, Minjie; Bai, Jing; Zhai, Yuchun ...

2019-10-28
Elsevier
https://doi.org/10.1016/j.matdes.2019.108288
Gu J, Yang S, Gao M, (2019) et al.,Micropore evolution in additively manufactured aluminum alloys under heat treatment and inter-layer rolling. Materials and Design, Volume 186, January 2019, Article number 108288

Downloaded from a DSpace repository. https://dspace.org/